Monte Carlo simulation studies of dendritic instabilities in three dimensions

Loki Jörgenson, R. Harris, Martin Grant, and Hong Guo

Department of Physics and Center for the Physics of Materials, McGill University, Rutherford Building,
3600 University Street, Montréal, Québec, Canada H3A 2T8

We extend our previous Monte Carlo studies of dendritic growth to the fully three-dimensional situation and demonstrate a Mullins-Sekerka instability due to the presence of a thermal gradient. We also study the thermal diffusion process associated with the instability, and identify important aspects of its role.

PACS number(s): 68.70.+w, 68.10.−m

I. INTRODUCTION

The Mullins-Sekerka instability and the complexities of dendritic growth have become an important topic in contemporary condensed-matter physics. They have been extensively discussed in the literature [1–4]. In this article, we describe the first Monte Carlo simulations of the Mullins-Sekerka instability in three dimensions (3D). Our article describes the application of a lattice-gas Monte Carlo algorithm to interfacial dynamics and makes contact with basic theory. Our present results deal entirely with two-dimensional interfaces in three space dimensions, so that the influences of lattice anisotropy and the roughening transition are implicitly included.

We first give an outline of our algorithm, which we have described in detail elsewhere [5]. We note that its applicability to dynamical problems has been well established [5, 6]. We also review the properties of our simple Hamiltonian, which models a system with first-order phase transition. We show how the latent heat of this transition enters in a natural way, and how it can be used to control the dynamics. We examine the ramifications of working with the simple cubic lattice and focus on configurations featuring a (111) interface. Typical dendrite simulations are shown and results are compared to basic theory. In the discussion, we compare and contrast our results with our previous data for two dimensions [5] and discuss the limitations of the current implementation of our model.

II. THE ALGORITHM AND THE HAMILTONIAN

The algorithm used is a variation of the deterministic Creutz demon algorithm. It has been discussed extensively in a previous publication [5] and will therefore only be outlined here.

The basic simulation system is a cubic lattice of N Ising spins. The lattice has periodic boundary conditions along the four sides, but the top and bottom of the system are maintained as if in contact with infinite heat baths at temperatures T_u and T_b. Each spin has two possible values $\sigma_i = \pm 1$ and an energy as defined by a Hamiltonian $H(\sigma_i)$ (see below). Associated with each spin is a demon carrying a non-negative amount of energy. Spin dynamics is implemented by inspecting the demon of a selected spin to see if it has the energy ΔE required to flip that spin. If the energy required is negative (energy is liberated), the spin flips and the energy is given to the demon. If the energy required is positive and less than the energy held by the demon, the spin flips and the energy is taken from the demon. If there is insufficient energy available for the flip, neither the spin nor the demon changes. The spin sites are visited in random order with one Monte Carlo step (MCS) being defined as N visits. The combined energy of the spin and demon systems is conserved but the spin number $\sum_{i=1}^{N} \sigma_i$ is not; this is in the universality class of model C of critical dynamics in the language of Hohenberg and Halperin [7].

Despite the discrete nature of the energy exchanges, it has been shown that each demon's energy distribution over time conforms to Boltzmann statistics [8]. Consequently, a local temperature can be assigned to each spin based upon its demon's average energy; the demon energy can be interpreted as the kinetic energy of a site in a vibrating lattice. As will be shown later, spatial averaging of the demon lattice provides a good measure of the local temperature at length scales larger than three lattice spacings despite the nonequilibrium nature of the simulation. At either end of the system, the heat baths are maintained by controlling the spin-flip dynamics with standard Metropolis techniques. In this way, a temperature gradient can be imposed across the entire system and the demon lattice then becomes the medium for thermal diffusion.

The energy of a spin is determined by the Hamiltonian

$$H = -J \sum_{\langle i,j \rangle} \sigma_i \sigma_j - \Delta \sum_i \sigma_i,$$

where $\sum_{\langle i,j \rangle}$ is over nearest neighbors and Δ is a uniform external field. Setting $\Delta = 0$ gives $H(\sigma_i)$ for the simple Ising model which has a second-order phase transition at $T_c \cong 4.541\, J$ (in 3D). The presence of Δ ensures that in the ground state, all spins σ_i have the value $+1$.

A latent heat is added to the system by defining each

spin state to be energetically degenerate; spin $\sigma_{\pm}$ has $\delta_{\pm}$ states of the same sign. This can be shown to introduce a first-order phase transition at temperature $T_m = 2\Delta/\ln(\delta)$ where δ is the ratio of degeneracies, $\delta = \delta_-/\delta_+$, and must be greater than 1. The latent heat Λ is then of order 2Δ.

Several other quantities are required to fully describe the Mullins-Sekeraka instability. The surface tension γ and its anisotropy in the three-dimensional nearest-neighbor Ising model is well defined [9]. The heat capacity C can be derived through mean-field theory and has been confirmed by simulation. The thermal diffusion constant D is more difficult to ascertain as it is the product of the particular spin-flip dynamics which couple the spin and demon systems. It must be determined empirically and it shows a strong temperature dependence, falling to zero very quickly with decreasing T. In Appendix A, we give typical values of all relevant parameters.

III. LATTICE GEOMETRIES

In an attempt to sample the range of instability phenomena exhibited by the lattice-gas model, a variety of approaches to modeling an unstable interface have been examined. Each has its advantages either in coding or in its relationship to a physical experiment. In all cases, the simulation model is a lattice of N Ising spins of dimension $N_x \times N_y \times N_z$. The thermal gradient is initially perpendicular to the interface and parallel to the z direction.

The simplest geometry is a simple cubic lattice with an interface initialized between two bulk phases and oriented along the [001] direction. An interface with this orientation has a roughening transition at a temperature $T_R \simeq 0.54 T_c$ [10]. This means that, at temperatures below T_R, the interface tends to form flat, facetted regions which are parallel to the initial interface [or the (100) and (010) planes]. These facets are surfaces of minimum energy which resist the formation of steps; the step free energy is nonzero below T_R and vanishes at the roughening transition. The *preferred* or *easy* directions of growth are those perpendicular to planes which have $T_R \equiv 0$. Consequently, any instability initiated on the (001) plane is subject to strong facetting; simulations carried out in this geometry rarely show any useful dynamics.

To overcome these difficulties within the simple cubic lattice, one alternative is to choose a (111) interface such that $T_R \equiv 0$. Details of the implementation are found in Appendix B. Growth along the [111] direction is preferred and, as expected, instabilities grow more easily, although they still exhibit some facetting in the 100 planes. However, the thermal gradient and the growth are not perpendicular to these planes and growth is not inhibited. Most of the results presented in this paper were produced using this geometry.

To make the algorithm reasonably efficient, the code makes use of large amounts of memory for spin and demon lattices, spin fields, site lists, and the like. Hardware memory limitations then restrict the maximum lattice size to systems of $128 \times 128 \times 96$ (1.5 million sites) or less.

$N_x = N_y = 128$ is uncomfortably close to the instability wavelength of the simulation (typically ≈ 40 lattice units), inviting interference from finite-size effects. In an effort to examine more accurately behavior at longer length scales, a variation of the (111) simple cubic geometry is used. It involves reducing N_x to a small number (typically $N_x = 8$) while increasing N_y and/or N_z appropriately. For example, systems of $8 \times 1024 \times 192$ have been used. We refer to such a configuration ($N_x \ll N_y$) as an example of *slab* geometry whereas a configuration with $N_x \equiv N_y$ is referred to as having *column* geometry.

There are also physical arguments which support the use of slab geometry. On the one hand, dendrite experiments with materials like succinonitrile are often carried out between flat surfaces, such as glass [11]. Although we recognize that there will be corrections due to the wetting of these surfaces by the liquid, we expect that the slab results will be of particular use when making comparisons to experiment.

IV. KINETICS OF AN UNSTABLE INTERFACE

The solid phase is initially set at the equilibrium melting temperature T_m while the liquid phase is supercooled at some temperature $T_u < T_m$; the interface is planar. The instability arises [2, 5, 4] from the competition between the inhomogeneous condensation of the unstable supercooled liquid phase onto the surface of the solid and the tendency of the interface to relax to its equilibrium configuration. The curvature of the interface is related to changes in the local temperature via the Gibbs-Thomson relation while its kinetics are controlled by thermal diffusion.

The diffusion mechanism is characterized by the length scale defined as $l \equiv 2D/v$, where D is the diffusion constant and v is the velocity of the almost planar interface in the direction of the initial thermal gradient. The time scale for thermal diffusion is assumed to be much shorter than the time scale for the interface dynamics; thus the thermal field is decoupled from the instability and is completely defined by the geometry of the local interface. In the very early time regime, linearizing the equations of motion, while omitting the damping due to surface tension, then gives a "dispersion relation" for the damped modes of the form

$$\omega(q) \equiv -\tau(q)^{-1} = \frac{2D}{l}q(1 - q^2 d_0 l)$$

where $d_0 = \gamma T_M C/\Lambda^2$ is the capillary length and where the q^3 term, which governs the relaxation of the interface, is the same as for the kinetics of the equilibrium interface. Within this linear approximation, therefore, there is a range of wave vectors for which ω is positive and which exhibit unstable behavior. The limit of instability is at $q_c = (d_0 l)^{-1/2}$, and the most unstable wave vector is $q_0 = (3d_0 l)^{-1/2}$. The characteristic length scale of the instability is therefore the geometric mean of the small and large length scales d_0 and l, respectively.

V. UNSTABLE INTERFACES

A. Results

We describe here the results of our simulation studies, including measurements of tip velocity, surface area, and power spectra from typical configurations. A qualitative description of the thermal fields is also provided to enhance understanding of the quantitative results.

As described above, a typical simulation run begins from a flat interface with a nondegenerate bulk phase initialized at T_m, the melting temperature and a degenerate bulk phase at an undercooled temperature $T_u < T_m$. The two bulk phases are configured with spin magnetizations as predicted for their respective temperatures (near ± 1 for most choices of T_m) by mean-field theory; their demons are initialized with the appropriate Boltzmann energy distributions. Fingerlike instabilities form immediately and quickly reach the asymptotic regime (typi-

FIG. 2.   A representation of a $128 \times 128 \times 96$ column system surface. The higher surfaces are shown in lighter greys. The image shown is for $t = 3000$ MCS.

cally within 400 Monte Carlo steps) where dendrite tip velocities are constant. The dendrites continue to grow and coarsen until the end of the run when they reach the far side of the system. Figure 1 shows a time series of cross-sectional slices from a slab system; the section shown is only a selected portion of the entire interface. Figure 2 shows a 3D representation of a column simulation at late time; note that dendrite growth is limited by the low ceiling on the system.

Tip velocity is measured by identifying the maximum height of the interface as a function of time; while not strictly exact, this technique is highly effective and quite accurate for measuring the primary instability. In the slab simulation, the tip velocity v is measured to be 3.1×10^{-2} in units of lattice spacings per MCS, for $400 \geq t \geq 1000$ MCS. This result, as shown in Fig. 3, is based on 29 trials of 2400 MCS each, using a $8 \times 1024 \times 96$ slab
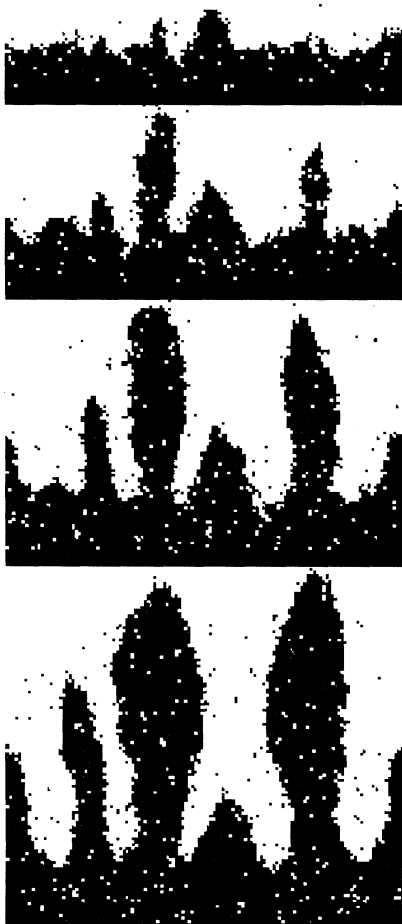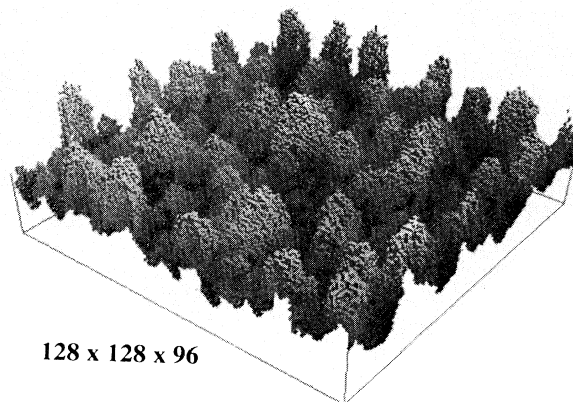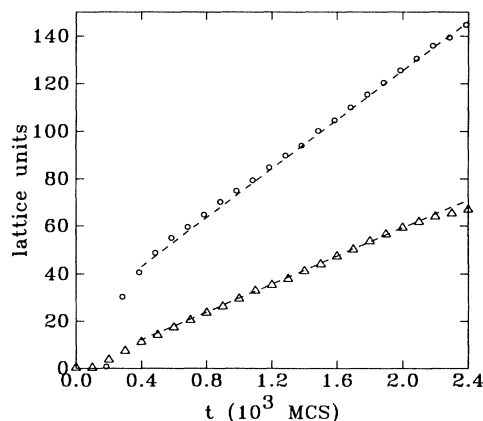
FIG. 1.   Time series of cross-sectional views of a slab system of dimension $8 \times 128 \times 92$. This is a subsection of the larger $8 \times 1024 \times 92$ system used to generate data. The images shown are for $t = 1000, 4000, 10\,000,$ and $26\,000$ MCS. The corresponding thermal field for $t = 25\,000$ MCS is shown in Fig. 11(d).

FIG. 3.   Maximum height (tip position) (○) and the (square root of the) total surface area (△) plotted against time t for a $8 \times 1024 \times 96$ slab system. The surface area is shown as $\sqrt{A(t) - A(200)}$ to highlight the t^2 growth, with $A(200)$ being $28\,249$ units. Data are averaged over 29 runs. The straight dashed lines are provided as references.

system with $T_u = 0.4T_c$, $T_m = 0.8T_c$, and $\delta = 2.8$. In the column system of $128 \times 128 \times 96$ with $T_u = 0.3T_c$, $T_m = 0.7T_c$, and $\delta = 2.8$, the tip velocity is measured to be 2.9×10^{-2} (Fig. 4); note that this is comparable to the slab value.

For both systems described above, the surface area grows with a t^2 power law appropriate to fingers growing at a constant rate from a 2D interface. This is also shown in Figs. 3 and 4. The tip radii ρ are of order of the unit lattice spacing ($\simeq 3$) and tend to fluctuate strongly due to the influence of roughening. We have found that measurements of ρ are insufficiently accurate for use in comparison with theories which relate ρ to v [13]. Likewise, there is insufficient flexibility in the parameters to test a significant range of v (see Appendix A).

The power spectra of both these systems have also been generated. The typical interface can have overhangs, bubbles, and pockets. These are presumed to be unimportant since they occur on length scales which are much shorter than the lengths of interest. They are therefore masked out by projecting the multi-valued interface onto the X-Y plane such that the interface is approximated by an isovalued surface. The slab surface is collapsed to a 1D interface by averaging along the shortest axis and treated by a Fourier transform to produce the power spectrum $P(\mathbf{q})$. The column surface is treated by a 2D Fourier transform and then averaged over all orientations of the vector $\mathbf{q}$. Figures 5 and 7 show the spectra $q^2 P(q)$ of the slab and column systems, respectively; they clearly show the mode of maximum instability q_0. The expected q^2 roughening contribution at large q is apparent as is the time-dependent relaxation of the roughening.

The slab spectra provide the best opportunity for comparison with two-dimensional systems [12, 5]. In Fig. 5, only the unstable modes below the roughening contin-

FIG. 5. The power spectra for a slab system scaled by q^2. The large-q end of the spectrum, showing the expected q^2 roughening modes, is excluded to display the unstable modes more clearly. Spectra for $t = 2400$ and 1600 MCS are shown.

uum are shown; they indicate a wavelength of maximum instability of $\lambda_0 \simeq 50$ lattice units with a secondary peak around 36 units. This is consistent with visual inspection (Fig. 1), which shows a typical separation between the instabilities of about 30–40 units. The same spectra are shown in Fig. 6, scaled with the square of time t^2; the fact that they are independent of time is consistent with the observation that the surface area is growing like t^2. The coarsening of the instabilities, as indicated by the lateral shift in the λ_0 peak, can be ignored as insignificant; in this respect, the data are very similar to that previously obtained for two-dimensional systems [5]. The features to the left of λ_0 are subharmonics of the primary and secondary instability peaks; they are located at $\lambda \simeq 66, 83, 100$, and 153 units.

The column power spectra, shown in Fig. 7, have better statistics, although it is clear that λ_0 is near the size of the system. In our experience, $128 \times 128 \times N_z$ is the
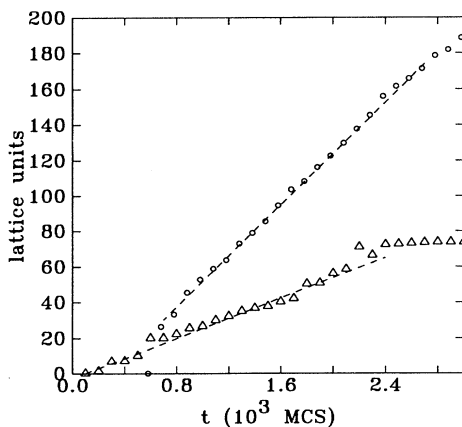

FIG. 4. Point of maximum height (tip position) (o) and the total surface area ($\triangle$) for a typical column system as a function of time. The surface area is shown as $\sqrt{A(t) - A(700)}$ to highlight the t^2 growth, with $A(700)$ being 42 693. The tip position saturates at late times as the tallest dendrite reaches the top of the system. Data are averaged over four runs. The straight dashed lines provided as references.
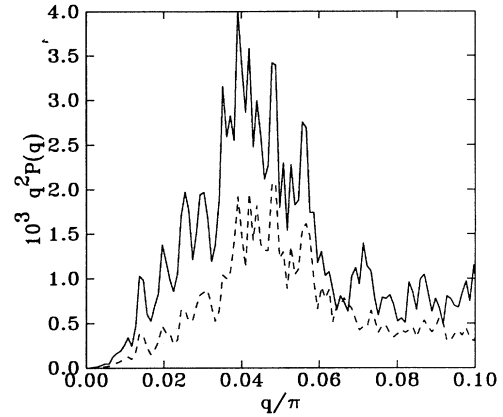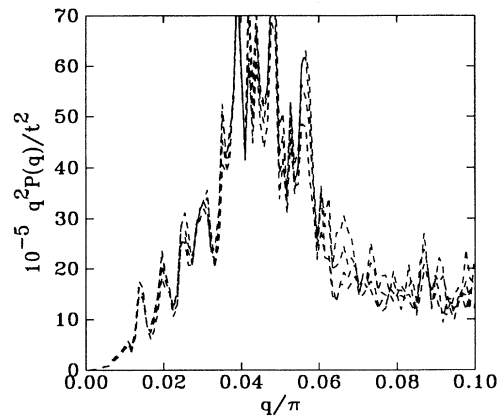

FIG. 6. The power spectra from Fig. 5 are shown scaled by t^2. Spectra are shown for t=2400, 2200, 2000, 1800, and 1600 MCS.
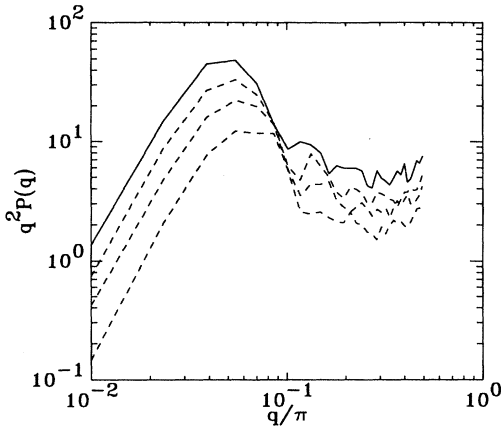
FIG. 7. The power spectra for a column system scaled by q^2 is shown in a log-log plot. Spectra for t=3000, 2600, 2200, and 1800 MCS are shown. Note the q^2 region at large q, indicative of roughening fluctuations, and the lateral shift of the mode of maximum instability.

FIG. 9. The radial structure factor from the time series shown in Fig. 8. The time is rescaled as $(t-t_0)^{0.5}$ to show the $t^{0.5}$ growth. The initial time $t_0 = 1000$ MCS is the time at which dendrites first intersect the cutting plane at $N_z = 72$.
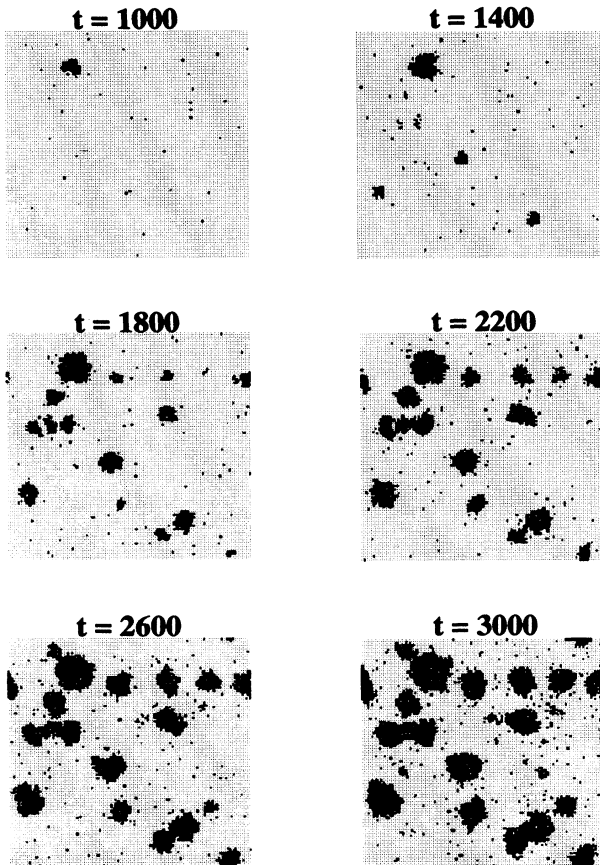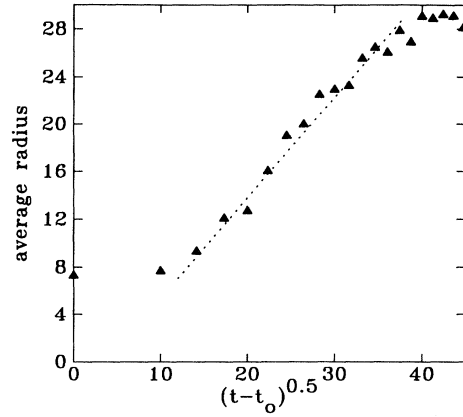

FIG. 8. A time series showing lateral cuts at fixed height across the growing dendrites in a column system. The dark areas are the solid dendrite(s).

minimum useful system size for the instabilities that we have been able to observe; results from systems of 64 × 64 × N_z clearly show the effects of finite size and are inappropriate for analysis. Consequently, this limits the height of the system permitted by hardware constraints to $N_z \approx 100$. The q_0 value is distinctly shifted in time by coarsening of the dendrites; this has been established by analyzing the perpendicular cross section of the interface profile at a fixed height. Figure 8 shows a times series of a typical cross section, starting from $t_0 = 1000$ MCS when the interface first intersects the plane. Figure 9 is the measured structure factor which is growing as a $t^{0.5}$. This is consistent with the geometric picture of the cross section of a parabola moving through a plane with constant velocity. The application of a simple scaling ansatz shows that the spectra are consistent with this behavior; the scaling is of the form
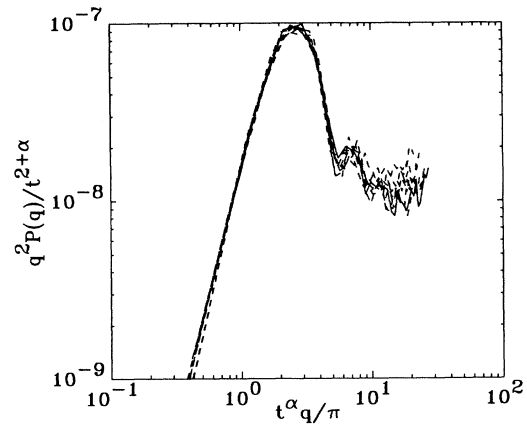

FIG. 10. The power spectra from Fig. 7 scaled by the ansatz $P(q,t) = t^{2+\alpha}\tilde{P}(qt^{\alpha})$. The figure shows a plot of $q^2\tilde{P}$ against qt^{α}. Spectra are shown for t=3000, 2800, 2600, 2400, 2200, 2000, 1800, and 1600 MCS.

$$P(q,t) = t^{2+\alpha} \tilde{P}(qt^{\alpha}),$$

where α is 0.5. To illustrate this, we show in Fig. 10 a plot of $q^2 \tilde{P}$ against qt^{α}.

B. Thermal diffusion

We have also analyzed the demon lattice for additional insight into the role of thermal diffusion. As described below, the local temperatures can be derived from the energy distribution of the demons by an appropriate coarse-grained average. Figure 11 shows a collection of thermal fields defined in this way: Each demonstrates some typical growth behavior based upon a specific choice of system parameters (latent heat, undercooling, melting temperature). The temperature range is represented from cold to hot by a contoured grey scale from black to white.
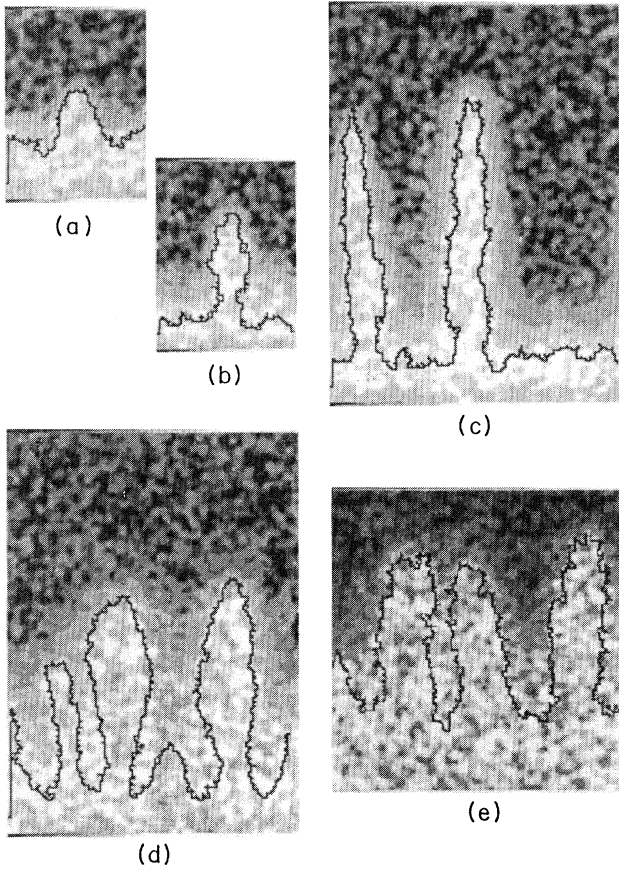

FIG. 11. Representative thermal fields derived from an analysis of cross-sectional slices of demon lattices. (a) and (b) are from column systems while (c)–(e) are from slab systems. The dark outline is the interface derived from the spin lattice. The lighter regions (on the bottom) are associated with the solid; above is the liquid. Temperature is shown as dark for cold and light for hot. The graininess of the temperature is related to the limited statistics of the demon distribution. Note that (d) is from the same simulation trial as shown in Fig. 1.

Fluctuations in the temperature on short length scales are due to the discrete nature of demon energy levels (spin flips are of order $\Delta\epsilon \simeq 2$ J) and the limited statistics of the demon lattice; each thermal image is based upon a simple Gaussian spatial-averaging scheme over the nearest 124 neighbors (i.e., a cube of $5 \times 5 \times 5$ centered on each site) with no time averaging. This is adequate to identify thermal gradients on length scales beyond three lattice spacings. The actual solid-liquid interface (derived from the spin lattice) is drawn over the field for reference.

Visual inspection identifies the presence of thermal gradients near the interfaces. As expected, the gradient between the liquid and solid bulk phases is strongest near the growing dendrite tips where the velocity is greatest. It is weaker along the nearly stationary initial interface. It is also evident that much of the liquid phase around the base of the dendrites has reached or exceeded the coexistence temperature. Indeed, where multiple dendrites appear, the region between them tends to fill with the excess latent heat produced by the moving interface. This excess is described by

$$\Gamma = C(T_m - T_u)/\Lambda,$$

where $\Gamma \equiv 1$ when the amount of latent heat released is identical to that required to heat the supercooled liquid to T_m; diffusion-limited processes require $\Gamma < 1$. As one of the dendrites begins to pull ahead of the others, it retards their growth by leaving its excess latent heat in their path, providing a natural selection mechanism (see Fig. 1).

Each of the images in the Fig. 11 gamut illustrates the effect of varying a particular system parameter (see Table I). Figure 11(a) is from a $64 \times 64 \times 96$ column system. Its melting temperature $T_m = 0.7T_c$ and undercooling $T_u = 0.3$ are typical midrange values; the degeneracy is low, $\delta = 3$, with a Γ value of 0.356. While this is much less than unity, this is relatively large for our model and it is reflected in the thermal field. There is little excess heat in front of the interface, which is advancing quite slowly. Figure 11(b) is for the same values of T_m and T_u but with $\delta = 5.7$ and $\Gamma = 0.29$. The abundance of latent heat has dramatically enhanced the instability and its accompanying thermal gradient. Figure 11(c) is from a $8 \times 128 \times 192$ slab system at $T_m = 0.65T_c$, $T_u = 0.2T_c$, and $\delta = 6$. It shows well-defined growth with little coarsening and limited diffusion into the bulk. Figure 11(d) shows a similar system with a higher undercooling $T_u = 0.3T_c$ and lower degeneracy $\delta = 4$; the consequent reduction in surface tension γ (see Table I) results in greater coarsening and the enhanced spin-flip activity increases thermal diffusion into the bulk. Figure 11(e) is also from a slab system; $T_m = 0.8$, $T_u = 0.4$, and $\delta = 2.8$. Like 11(a), this system has a high Γ (small excess heat), but the lower surface tension due to higher operating temperatures results in increased interface dynamics. Figures 11(b) and 11(e) correspond to the data presented in Sec. V A.

In addition to confirming the diffusive nature of our model, these images provide invaluable commentary on how the diffusion is taking place. In particular, it is apparent that the diffusion occurs on time scales much

longer than the spin dynamics. This is evident in Figs. 11(a) and 11(c) where a dark band of solid appears near the bottom boundary. The brighter band above is at a higher temperature due to excess heat produced by the passing of the interface. In these systems, $\Gamma \ll 1$ and clearly the excess heat has not had time to diffuse to the cooler region below. This implies that the processes represented here are far from the *quasistatic* limit. Figure 11(a) demonstrates a related shortcoming of our model; diffusion into the undercooled bulk is also extremely slow. Although the hot solid is moving slowly, the heat is not being transferred into the liquid at a detectable rate; the gradient is largely restricted to the range of the spin interactions at the interface.

Both of these situations are manifestations of the same fact: One of the characteristics of the lattice-gas model is that it is typically quite *stiff* and thermal diffusion occurs on time scales much longer than the interface dynamics, especially in the melt where low temperatures reduce diffusion further. Thus our model has only a limited ability to properly represent thermal diffusion. The rate of diffusion is directly tied to the rate of spin-flip dynamics. At temperatures near T_m, the diffusion process is occurring on time scales which are at best comparable to the interface growth whereas at colder temperatures, spin-flips become infrequent and diffusion almost ceases to exist. Since most theoretical and experimental results are based on the quasistatic assumption which presumes thermal fields to always be in equilibrium, contact with our simulation results is therefore difficult.

The absence of sidebranching in any of our simulations is related to the geometry of the system. On the one hand, this has to do, again, with the limited nature of the diffusion. In the column geometry, the maximum lattice size provides insufficient space for more than one dendrite; the sides of the growing structure "see" themselves through the periodic boundaries, and secondary instabilities are suppressed by the presence of excess thermal energy. Multiple dendrites are relatively rare and tend to obstruct one another for the same reasons. On the other hand, the anisotropy in the surface tension γ can also play a key role. Thus, in slab systems, although finite size is not an issue, growth is complicated by the orientation of the lattice. Only one of the three preferred directions of growth is coplanar with the slab (i.e., the [111] direction perpendicular to the initial interface). Consequently, even well-defined gradients like those seen in Fig. 11(c) are ineffective at inducing secondary instabilities along the sides. In both cases, an accelerated diffusion process is expected to improve the situation by removing excess heat and enhancing the local thermal gradient.

VI. DISCUSSION

We have shown our instabilities to have the identifiable characteristics of dendritic growth: consistent physical appearance, constant tip velocity, measurable instability modes with a distinct maximum at q_0, and scalable power spectra. The form of the scaling ansatz is simple and easily related to the geometry of the system.

The results presented in our paper establish the algorithm as a useful technique for the study of the Mullins-Sekerka instability in three dimensions. We have simulated dendritic growth which, with the exception of sidebranching, exhibits all the behavior seen in physical experiments, and we have shown that the growth can be observed in a variety of relevant experimental configurations. Our study of the thermal fields has clearly demonstrated the role of thermal diffusion in controlling the instability.

APPENDIX A: TYPICAL MODEL PARAMETERS

Melting temperatures T_m were chosen around $0.7T_c$ (of the Ising model) to enhance the dynamics, and undercooled temperatures in the unstable systems were normally around $0.3T_c$. Field strengths were of order of $\Delta \sim J$, so that degeneracies were in the range 2–5. With these values, typical values of the capillary length d_0 and the diffusion length l can be derived.

As defined in the text, the capillary length is

$$d_0 = \gamma T_m C / \Lambda^2,$$

where γ is the surface tension, T_m the melting temperature, C the specific heat capacity of the bulk phases, and Λ the latent heat. Of these parameters, T_m and Λ are explicitly known, γ can be measured directly by simulation [9], and C can either be measured by simulation [8] or taken from the mean-field expression. Table I is provided to give a quantitative sense of the parameter space available. The entries demonstrate the range of parameters for systems which have shown dendritic behavior; these values are specifically for the systems which generated Figs. 11(a)–11(e), respectively. They are based upon mean-field values for C.

TABLE I. The table entries show the range of system parameters which demonstrate dendritic behavior; they correspond to the thermal images in Fig. 11, in order (a) to (e). The units of T_m are in T_c of the unmodified Ising model; Λ is in units of J; δ, C, and Γ are dimensionless; d_0 is in lattice spacings.

T_m	Λ	δ	C	γ	d_0	Γ
0.7	3.5	3.0	0.68	1.2	0.21	0.36
0.7	5.5	5.7	0.86	1.2	0.11	0.29
0.65	5.3	6.0	0.70	1.1	0.081	0.27
0.65	4.1	4.0	0.60	1.1	0.12	0.23
0.8	3.7	2.8	1.0	1.0	0.26	0.49

The diffusion length is defined to be $l = 2D/v$, where v is the measured velocity of the unstable interface and D is the diffusion constant. In the limit of $l \to \infty$, the time scale of thermal diffusion is much shorter than that for the motion of the interface, and one approaches the quasistatic limit. The diffusion length can be measured in a number of ways [5]. The most direct method is to visually inspect or measure the gradient in the thermal field ahead of the advancing interface. Linear theory [2] predicts a simple form for the gradient which is assumed to be perpendicular to a flat interface:

$$u(z) = e^{-2z/l} - 1, \quad z \geq 0 \text{ (liquid)},$$

where $u \equiv (T - T_m)C/\Lambda$ and $z = 0$ is the position of the interface. The width of the gradient from T_m to T_u is thus of order l. This result presumes the quasistatic limit. In the slab systems [Figs. 11(c)–11(e)], l at the dendrite tips around 15 units. In the column systems, l is approximately 5 and 9 units for Figs. 11(a) and 11(b), respectively. Note that there are also gradients clearly present in Fig. 11(c) along the sides of the dendrites and at the initial interface. These show larger values for l. One can conclude from this that the quasistatic limit is not applicable since one cannot otherwise explain the different values of l for equivalent interfaces.

APPENDIX B: CODING OF LATTICE GEOMETRY

In all cases, the algorithm uses a virtual lattice which is regular and cubic with $N_x \times N_y \times N_z$ sites; the choice of *nearest neighbors* and spin bond strengths determines which physical crystal structure the algorithm emulates. The initial interface is always parallel to the X-Y plane of the virtual lattice. The "sides" of the system are always periodic; the "ends" are pinned and controlled by infinite heat baths.

In the case where the nearest neighbors of a site at i, j, k are defined as the adjacent sites along the Cartesian axes (i.e., $i \pm 1, j \pm 1, k \pm 1$) and bond strengths are equal and identical to J of the Hamiltonian, the system represents the simple cubic (sc) structure.

If the nearest neighbors are specially chosen triplets in the X-Y planes above and below the site (i.e., $i_1, j_1, k - 1$; $i_2, j_2, k - 1$; $i_3, j_3, k - 1$; $i_4, j_4, k + 1$; $i_5, j_5, k + 1$; $i_6, j_6, k + 1$) and bond strengths are equal, the lattice represents the sc structure oriented with the (111) plane parallel to the X-Y plane. Each X-Y plane k defines the triplet neighbors for a site differently according to its designation as one of the three distinct laterally displaced sc (111) planes; the sc structure is constructed by stacking these X-Y planes cyclically (i.e., 1,2,3,1,2,3,1,...).

[1] H. van Beijeren and I. Nolden, in *Topics in Current Physics*, edited by W. Schommers and P. von Blackenhagen (Springer-Verlag, Berlin, 1987), Vol. 43, p. 259; J.D. Weeks, in *Ordering in Strongly Fluctuating Condensed Matter Systems*, edited by T. Riste (Plenum, New York, 1980); J.D. Weeks and G.H. Gilmer, Adv. Chem. Phys. **40**, 157 (1979).

[2] J.S. Langer, Rev. Mod. Phys. **52**, 1 (1980).

[3] J.S. Langer, in *Lectures in the Theory of Pattern Formation, Chance and Matter*, Proceedings of the Les Houches Summer School Session 4b, edited by J. Souletie, J. Vannumenus, and R. Stora (North-Holland, Amsterdam, 1986); D. Kessler, J. Koplik, and H. Levine, Adv. Phys. **37**, 255 (1988).

[4] D. Kessler, J. Koplik, and H. Levine, Adv. Phys. **37**, 255 (1988)

[5] R. Harris, L. Jörgenson, and M. Grant, Phys. Rev. A **45**, 1024 (1992).

[6] L. Jörgenson, R. Harris, and M. Grant, Phys. Rev. Lett. **63**, 1693 (1989).

[7] P.C. Hohenberg and B.I. Halperin, Rev. Mod. Phys. **49**, 435 (1977).

[8] R. Harris and M. Grant, Phys. Rev. B **38**, 9323 (1988).

[9] K. Mon and D. Jasnow, Phys. Rev. A **30**, 670 (1984).

[10] K. Mon, D. Landau, and D. Stauffer, Phys. Rev. B **42**, 545 (1990).

[11] X.W. Qian and H.Z. Cummins, Phys. Rev. Lett. **64**, 3038 (1990).

[12] R. Harris and M. Grant, J. Phys. A **23**, L567 (1990).

[13] J. Langer and H. Müller-Krumbhaar, Acta Metall. **26**, 1681 (1978); **26**, 1689 (1978); **26**, 1697 (1978).
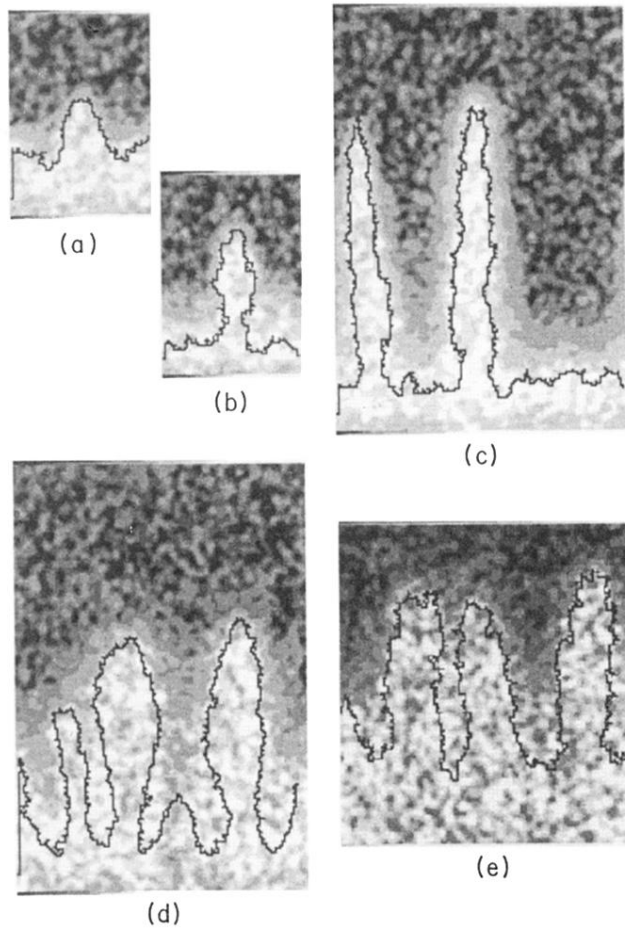
FIG. 11. Representative thermal fields derived from an analysis of cross-sectional slices of demon lattices. (a) and (b) are from column systems while (c)–(e) are from slab systems. The dark outline is the interface derived from the spin lattice. The lighter regions (on the bottom) are associated with the solid; above is the liquid. Temperature is shown as dark for cold and light for hot. The graininess of the temperature is related to the limited statistics of the demon distribution. Note that (d) is from the same simulation trial as shown in Fig. 1.
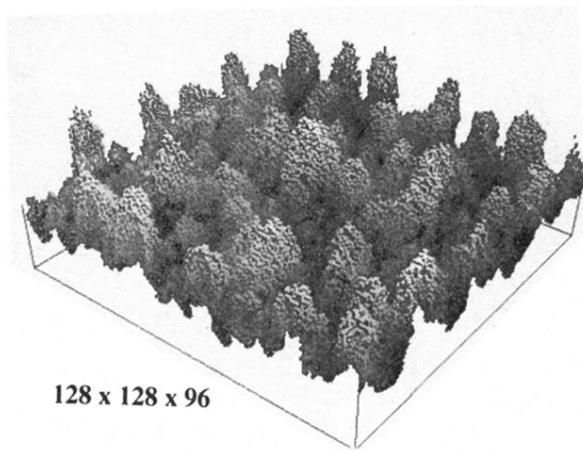
128 x 128 x 96

FIG. 2.   A representation of a $128\times128\times96$ column system surface. The higher surfaces are shown in lighter greys. The image shown is for $t = 3000$ MCS.